

Supporting Information

Two-dimensional layered Dion-Jacobson phase organic-inorganic tin iodide perovskite field-effect transistors

Hongyu Ji, Xin Liu, Longtao Li, Fan Zhang, Liang Qin, Zhidong Lou[□], Dan Li[□],

Yufeng Hu, Yanbing Hou, and Feng Teng[□]

Key Laboratory of Luminescence and Optical Information, Ministry of Education,

Beijing Jiaotong University, Beijing 100044, China

E-mail addresses: zhdlou@bjtu.edu.cn, danli@bjtu.edu.cn, and fteng@bjtu.edu.cn

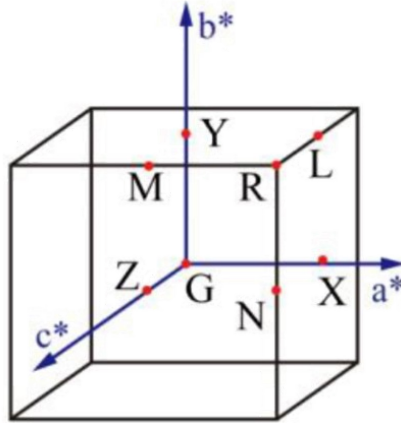


Figure S1. Simplified Brillouin zone for BDASnI₄ with high-symmetry k -points. R is the starting point. K_{R-M} , K_{R-N} , and K_{R-L} are the three basic vectors along the a -, b -, and c -axes, respectively.

Table S1. Calculated unit-cell parameters of BDASnI₄. a , b , and c represent the lattice constants in the directions of the base vectors, and α , β , and γ are the angles between them.

| Perovskite | a (Å) | b (Å) | c (Å) | α (°) | β (°) | γ (°) |
|---------------------|---------|---------|---------|--------------|-------------|--------------|
| BDASnI ₄ | 6.20 | 6.15 | 10.49 | 80.93 | 95.45 | 87.08 |

Table S2. Calculated bond lengths and bond angles of the [SnI₆]⁴⁻ octahedra in

BDASnI₄. The bonds shown in Figure 1a are classified into the in-plane and out-of-plane ones, which are within and vertical to the inorganic layers, respectively.

| Label | BDASnI ₄ | |
|----------------------|---------------------|-------|
| Sn-I bond length (Å) | In-plane | 3.088 |
| | Out-of-plane | 3.158 |
| | Average | 3.123 |
| I-Sn-I angle (°) | In-plane | 179.2 |
| | Out-of-plane | 179.1 |
| | Average | 179.2 |
| Sn-I-Sn angle (°) | In-plane | 179.2 |
| | Out-of-plane | - |
| | Average | - |

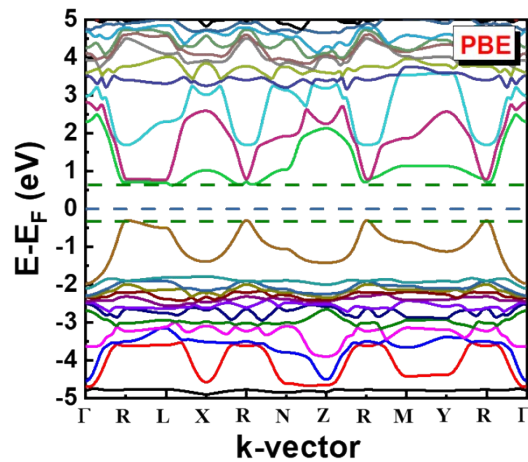


Figure S2. Electronic band structure of BDASnI₄ calculated using PBE functional.

Calculations of effective mass, mobility, and exciton binding energy

The charge carrier effective masses and intrinsic mobilities of BDASnI₄ were studied to evaluate the charge carrier transport characteristics. In most semiconductors, the HSE calculations do not change the band energy dispersion relations obtained from the PBE calculations.^{1, 2} Therefore, to avoid the high computational cost of

HSE43+SOC, the effective masses of electrons and holes of BDASnI₄ in different directions were estimated by the curvatures of the conduction band minimum (CBM) and valence band maximum (VBM) based on the band structure calculated with the PBE scheme using the following expression:³

$$m^* = \hbar^2 \left(\frac{\partial^2 \varepsilon(k)}{\partial^2 k^2} \right)^{-1} \quad (\text{S1})$$

where \hbar is the reduced Planck constant, k is the wavevector, and $\varepsilon(k)$ is the eigenvalue of the band edge around CBM and VBM. Using a simple approach based on the deformation potential theory, the intrinsic electron and hole mobilities of BDASnI₄ along the base vector directions in the first Brillouin zone were derived theoretically by:^{4,5}

$$\mu = \frac{(8\pi)^{1/2} \hbar^4 q C_{ii}}{3(m^*)^{5/2} (k_B T)^{3/2} E_1^2} \quad (\text{S2})$$

where q is the elementary charge; k_B is the Boltzmann constant; T is the temperature set at 300 K; E_1 is the deformation potential for electrons or holes and C_{ii} is the elastic matrix constant,^{6,7} both of which can be acquired by the first-principles computations. Additionally, the exciton binding energy (E_B) plays a key role in discriminating whether charge carriers behave as free particles or as bound excitons. Using a modified hydrogen-atom-like Bohr model based on the effective mass theory in 3D hybrid perovskite materials,⁸ the Wannier-Mott exciton binding energy of BDASnI₄ was calculated according to the equation:

$$E_B = \frac{m_r^* q^4}{32\pi^2 \epsilon^2 \hbar^2} \quad (\text{S3})$$

where ϵ is the dielectric constant of BDASnI₄ (5.579) calculated by the density functional perturbation theory; $m_r^* = (m_e^* \times m_h^*) / (m_e^* + m_h^*)$, is the reduced effective mass of the exciton with the average values of electron and hole effective masses m_e^* and m_h^* .

Table S3. Calculated electron and hole effective masses of BDASnI₄ along the seven highly symmetric k -directions in the simplified Brillouin zone with the static mass m_0 of an electron as the unit. The values are averaged along the in-plane (K_{R-M} and K_{R-N}) and out-of-plane (K_{R-L} , K_{R-X} , K_{R-Y} , K_{R-Z} , and K_{R-G}) directions, respectively. Herein, K_{R-X} , K_{R-Y} , K_{R-Z} , and K_{R-G} between the inorganic layers are included in the out-of-plane direction.

| Perovskite | $m^* (m_0)$ | K_{R-M} | K_{R-N} | K_{R-L} | K_{R-X} | K_{R-Y} | K_{R-Z} | K_{R-G} | In-plane | Out-of-plane |
|---------------------|-------------|-----------|-----------|-----------|-----------|-----------|-----------|-----------|----------|--------------|
| BDASnI ₄ | m_e^* | 0.119 | 0.274 | 1.581 | 0.453 | 0.120 | 0.212 | 0.271 | 0.197 | 0.527 |
| | m_h^* | 0.172 | 0.146 | 0.307 | 0.148 | 0.178 | 0.153 | 0.165 | 0.159 | 0.190 |

Table S4. Calculated electron and hole mobility values of BDASnI₄ in the base vector directions. E_{1c} and E_{1v} are the deformation potentials for electrons and holes, respectively, and C_{ii} is the elastic constant.

| Perovskite | Direction | E_{1c} (eV) | E_{1v} (eV) | C_{ii} (Kbar) | μ_e (cm ² V ⁻¹ s ⁻¹) | μ_h (cm ² V ⁻¹ s ⁻¹) |
|---------------------|----------------------|---------------|---------------|-----------------|--|--|
| BDASnI ₄ | In-plane (a) | -8.328 | -8.436 | 275.20 | 4986.7 | 1934.9 |
| | In-plane (b) | -5.904 | -9.240 | 254.85 | 1142.2 | 2249.9 |
| | Out-of-plane (c) | -9.080 | -14.274 | 230.44 | 5.5 | 133.0 |
| | In-plane (average) | | | | 3064.5 | 2092.4 |

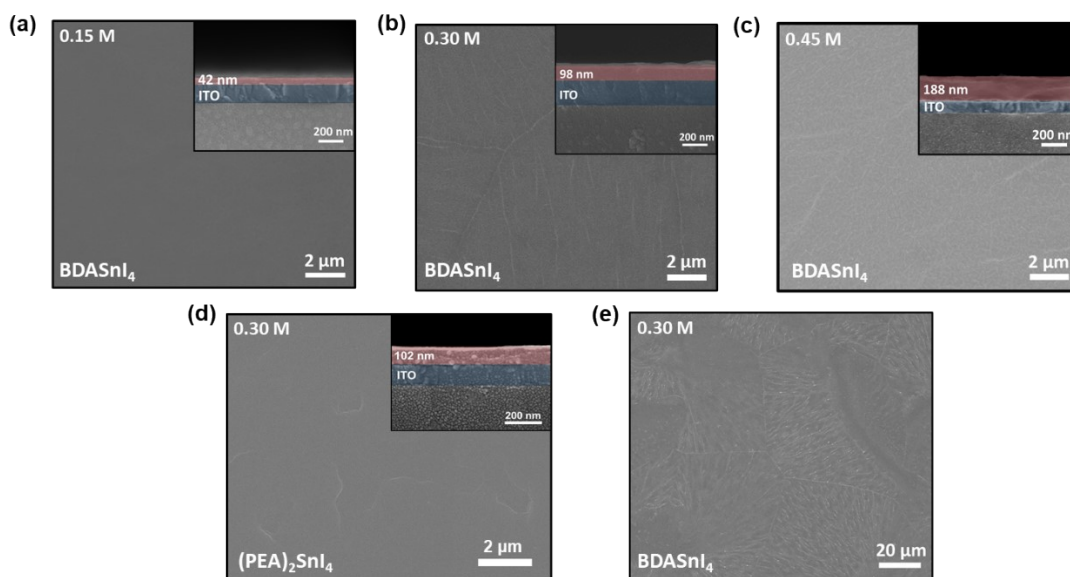


Figure S3. Top-view and cross-sectional SEM images of BDASnI_4 thin films prepared at the precursor solution concentrations of (a) 0.15, (b) 0.30, and (c) 0.45 M on ITO/glass substrates, respectively. (d) Top-view and cross-sectional SEM images of $(\text{PEA})_2\text{SnI}_4$ thin film. (e) Large-scale top-view SEM image of BDASnI_4 film prepared at a precursor solution of 0.3 M on an ITO/glass substrate. All the BDASnI_4 and $(\text{PEA})_2\text{SnI}_4$ thin films were spin coated at 4000 rpm.

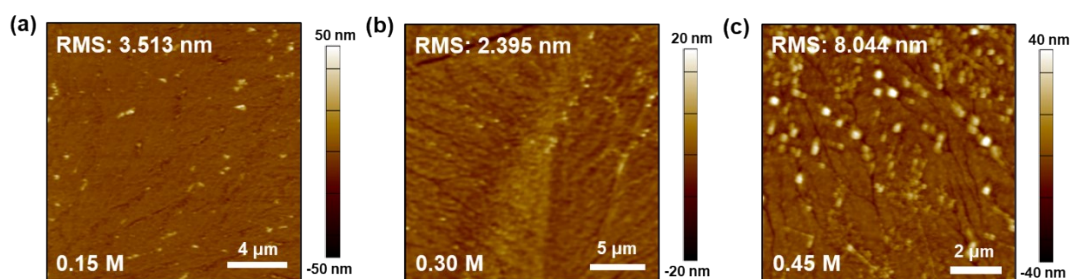


Figure S4. AFM images of BDASnI_4 thin films prepared at the precursor solution concentrations of (a) 0.15, (b) 0.30, and (c) 0.45 M on ITO/glass substrates, respectively.

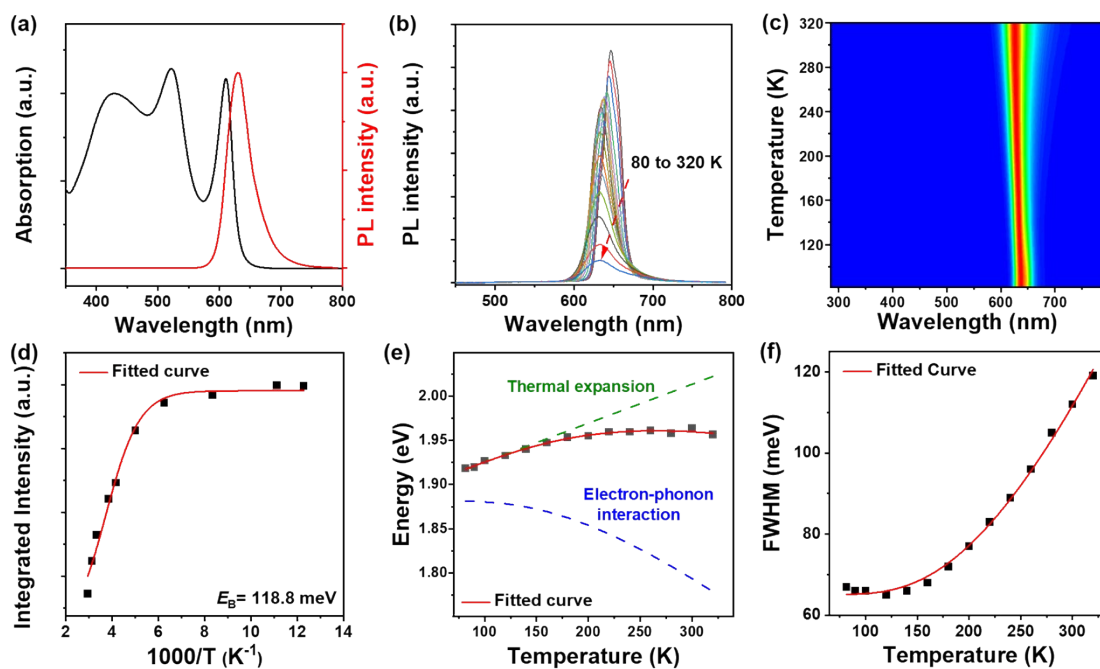


Figure S5. Optical properties and electron-phonon interaction of $(\text{PEA})_2\text{SnI}_4$ thin films. (a) Room-temperature UV-vis absorption and PL spectra and (b) temperature-dependent PL spectra. (c) Pseudo-color map of the temperature-dependent PL spectra. (d) Integrated PL intensity as a function of the inverse of temperature. (e) Evolution of the PL peak energy (bandgap) with temperature. The calculated individual contributions from the thermal expansion and electron-phonon interaction are depicted by the dashed lines. (f) Evolution of the FWHM of the PL peak with temperature.

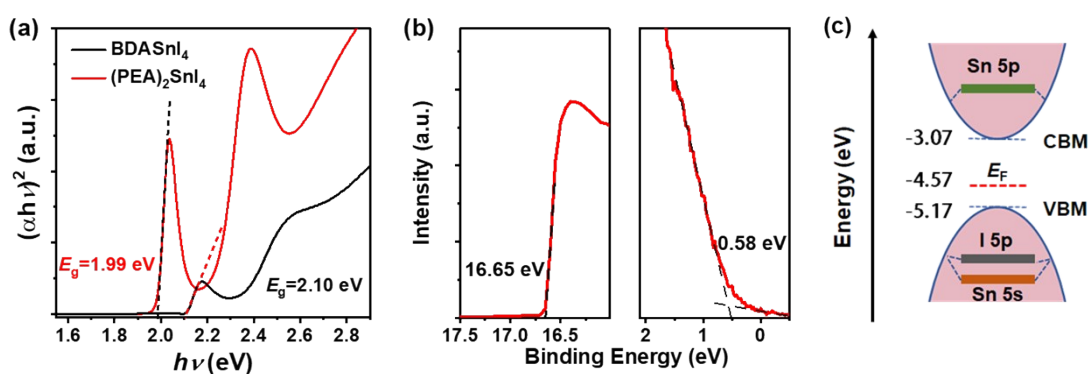


Figure S6. (a) Tauc plots of the absorption spectra of BDASnI_4 and $(\text{PEA})_2\text{SnI}_4$ thin films. (b) UPS spectrum of BDASnI_4 thin film. (c) Schematic of the electronic energy band of BDASnI_4 thin film.

Fermi level position

The work function (φ) of a semiconductor material, which is defined as the energy difference between the vacuum level and the Fermi energy level (E_F), can be extracted from its ultraviolet photo-electron spectrum (UPS) spectrum in binding energy scale using the following expression: ⁹

$$\varphi = h\nu - E_{cutoff} \text{ (S4)}$$

where $h\nu$ is the photon energy of the UV source of the He-I UPS (21.22 eV), and E_{cutoff} is the cut-off energy of the secondary electron emission. The vacuum level is generally set to zero, thus, the Fermi level can be calculated by $E_F = 0 - \varphi = E_{cutoff} - h\nu$. In this work, the Fermi level of the BDASnI₄ thin film is estimated to be -4.57 eV since the E_{cutoff} is 16.65 eV.

Exciton lifetime

A low-dimensional layered perovskite is recognized as a strongly confined system with a large exciton binding energy due to the quantum and dielectric confinements,¹⁰ whose PL behavior is determined by the recombination dynamics of excitons. To extract the exciton lifetime of a perovskite accurately, its time-resolved photoluminescence (TRPL) decay curve is generally fitted with the following three-variable parameter exponential function:¹¹

$$I(t) = A_1 \exp\left(-\frac{t}{\tau_1}\right) + A_2 \exp\left(-\frac{t}{\tau_2}\right) + A_3 \exp\left(-\frac{t}{\tau_3}\right) \text{ (S5)}$$

and the average exciton lifetime (τ_{ave}) is obtained by:

$$\tau_{ave} = \frac{A_1 \tau_1^2 + A_2 \tau_2^2 + A_3 \tau_3^2}{A_1 \tau_1 + A_2 \tau_2 + A_3 \tau_3} \text{ (S6)}$$

where τ_i refers to the time constant of each exponential component; A_i is the preexponential factor for each component. In this model, there exist three physical processes dominating the exciton recombination: trap-related non-radiative recombination, radiative recombination, and Auger recombination, which are represented by the longest (τ_1), medium (τ_2), and shortest (τ_3) lifetimes, respectively.^{10, 12} In theory Auger recombination is relatively severe in 2D perovskites compared to 3D perovskites because of the larger exciton binding energy and higher carrier density at the recombination center due to the quantum confinement effect in the multi-wells naturally formed by organic and inorganic layers.¹⁰

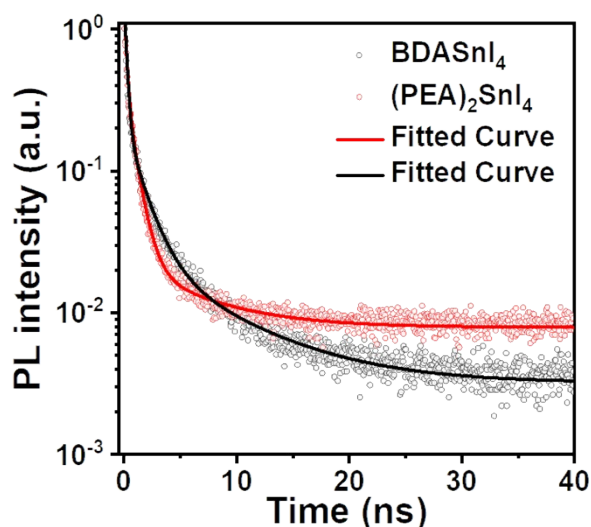


Figure S7. TRPL spectra of BDASnI₄ and (PEA)₂SnI₄ thin films fitted with a three-exponential decay model.

Table S5. Exciton lifetimes of BDASnI₄ and (PEA)₂SnI₄ thin films.

| Perovskite | τ_1 (ns) | τ_2 (ns) | τ_3 (ns) | $\tau_{average}$ (ns) |
|-------------------------------------|---------------|---------------|---------------|-----------------------|
| BDASnI ₄ | 7.30 | 1.46 | 0.21 | 2.14 |
| (PEA) ₂ SnI ₄ | 6.20 | 0.80 | 0.19 | 1.43 |

Experimental exciton binding energy

The exciton binding energy of a perovskite is usually evaluated by the quenching of the integrated PL intensity with increasing temperature, which is described by the Arrhenius equation:¹³

$$I(T) = \frac{I_0}{1 + Ae^{-E_B/k_B T}} \quad (\text{S7})$$

where I_0 is the integrated PL intensity at 0 K and A is a constant.

Table S6. Extracted parameters from fitting the temperature-dependent PL peaks of BDASnI₄ and (PEA)₂SnI₄ thin films in Figure 2e and S5e. $\Delta_{EP} = E_{EP}(320 \text{ K}) - E_{EP}(80 \text{ K})$, which represents the contribution of the electron-phonon interaction to the temperature dependence of the bandgap over the temperature range from 80 to 320 K.

| Perovskite | E_0 (eV) | A_{TE} (meV/K) | A_{EP} (meV) | E_{LO} (meV) | Δ_{EP} (meV) |
|-------------------------------------|------------|------------------|----------------|----------------|---------------------|
| BDASnI ₄ | 2.45 | 0.05 | -365.12 | 99.89 | -20.07 |
| (PEA) ₂ SnI ₄ | 2.22 | 0.44 | -338.41 | 67.21 | -64.83 |

Table S7. Extracted parameters from fitting the temperature-dependent FWHMs of BDASnI₄ and (PEA)₂SnI₄ thin films in Figure 2f and S5f.

| Perovskite | Γ_{inh} (meV) | Γ_{LO} (meV) | $\hbar\omega$ (meV) |
|-------------------------------------|----------------------|---------------------|---------------------|
| BDASnI ₄ | 60.39 | 544.85 | 56.81 |
| (PEA) ₂ SnI ₄ | 65.08 | 565.83 | 66.61 |

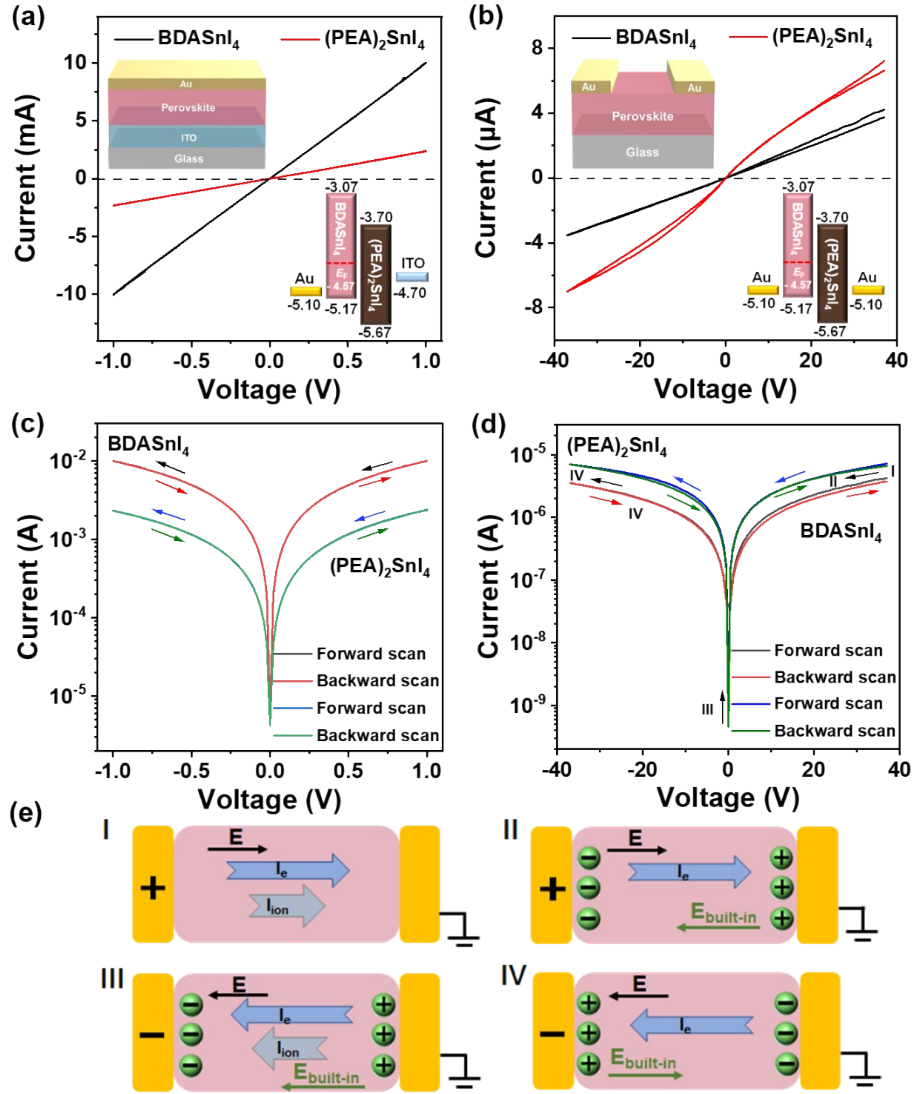


Figure S8. Current-voltage curves for the (a) vertical and (b) lateral two-terminal devices based on BDASnI₄ and (PEA)₂SnI₄ thin films with the voltage sweeping forward from positive to negative and then reverse to positive. The insets show the device structures and energy level alignments. In the lateral devices the Au electrode separation is 50 μm. The measurements were performed in a N₂-filled gloved box at room temperature under dark conditions to exclude the influence of environmental factors. (c) and (d) Semilogarithmic plots of (a) and (b). The overlapping forward and reverse currents in (c) suggest the out-of-plane ion migration in the BDASnI₄ and (PEA)₂SnI₄ films is suppressed by the bulky organic layers. The nonoverlapping forward and reverse currents in (d) is indicative of the in-plane ion migration in the two perovskite films. (e) Schematic diagrams of the lateral two-terminal perovskite devices showing the in-plane ion migration and accumulation at the electrodes and its influence on the dual-sweep current-voltage curves of the devices. E and E_{built-in} stand

for the applied electric field and the built-in electric field by ions. I_e and I_{ion} are electronic and ionic currents. The four stages are labeled for the current-voltage curves of the lateral two-terminal BDASnI₄ device in (d).

Table S8. Conductivity values and ion migration of BDASnI₄ and (PEA)₂SnI₄ thin films.

| Perovskite | Direction | Conductivity (Scm ⁻¹) | Ion migration |
|-------------------------------------|--------------|-----------------------------------|---------------|
| BDASnI ₄ | In-plane | 5.7×10^{-4} | Yes |
| | Out-of-plane | 9.9×10^{-6} | No |
| (PEA) ₂ SnI ₄ | In-plane | 6.1×10^{-6} | Yes |
| | Out-of-plane | 3.5×10^{-6} | No |

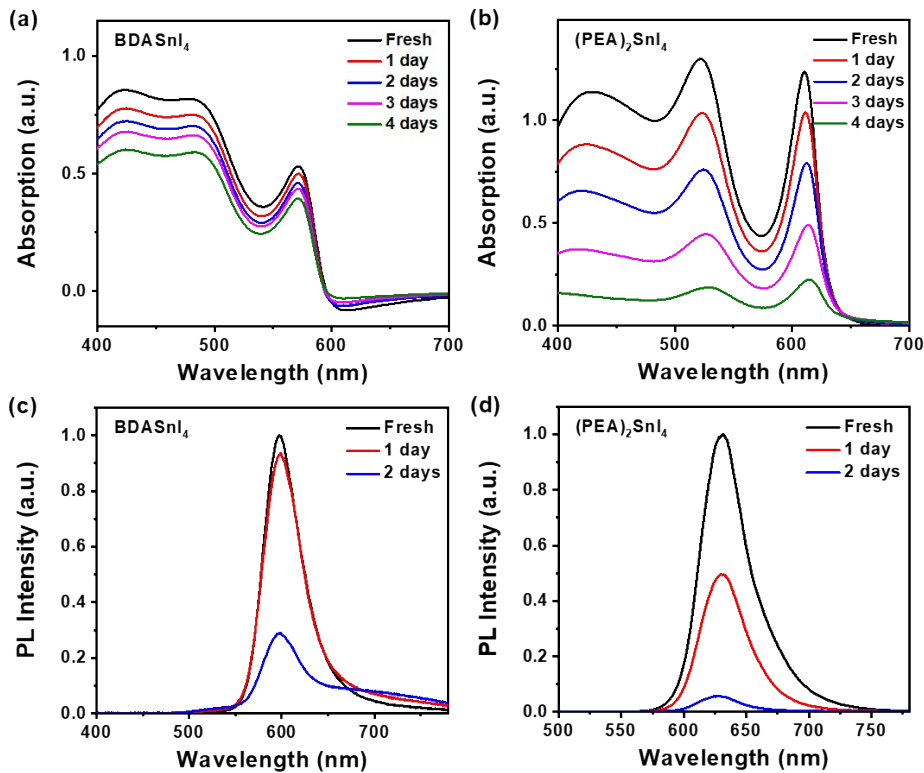


Figure S9. Comparison between the environmental stability of perovskite thin films in air with a relative humidity of 28% at 292 K under dark conditions. Variation of the absorption spectra of (a) BDASnI₄ and (b) (PEA)₂SnI₄ films over time. Variation of the normalized PL spectra of (c) BDASnI₄ and (d) (PEA)₂SnI₄ films over time.

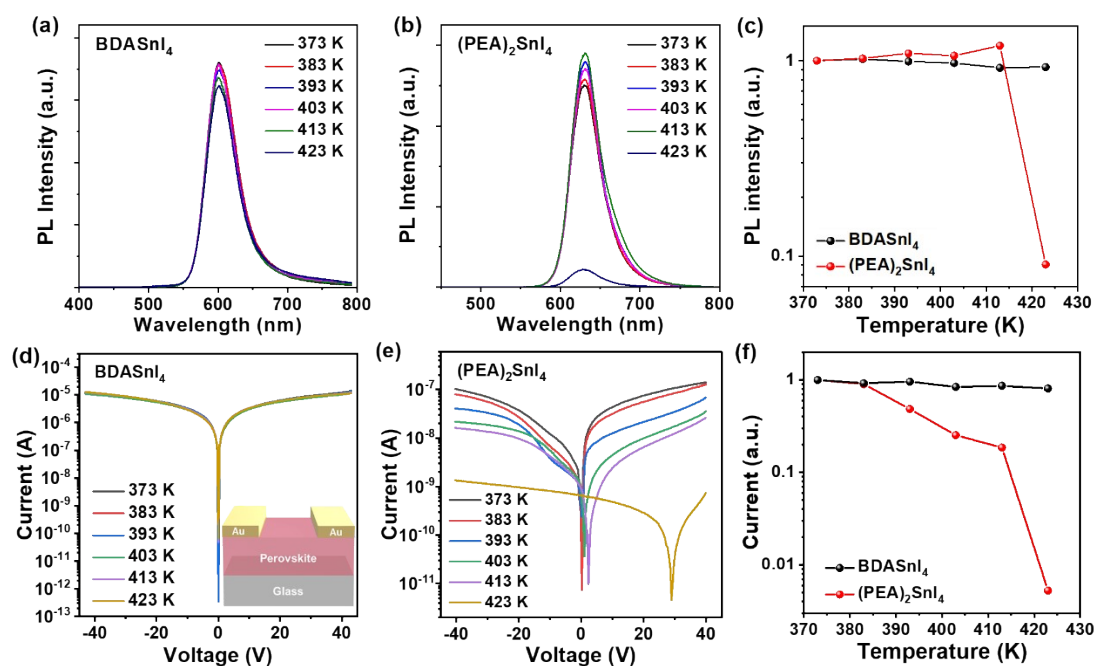


Figure S10. Comparison between the thermal stability of perovskite thin films. The as-prepared perovskite thin films were placed on a hot plate in a N_2 -glove box for 10 min at different temperatures for additional thermal treatments before the corresponding characterizations. Variation of the PL spectra of (a) $BDASnI_4$ and (b) $(PEA)_2SnI_4$ thin films with temperature and (c) PL intensity of the films as a function of temperature. Variation of the currents of the lateral two-terminal (d) $BDASnI_4$ and (e) $(PEA)_2SnI_4$ thin film devices with temperature and (f) current of the films as a function of temperature. The inset in (d) illustrates the structure of the two-terminal lateral perovskite devices.

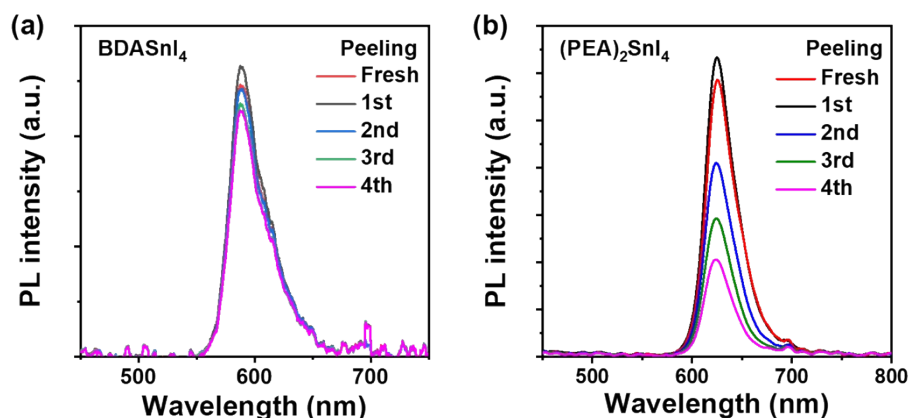


Figure S11. Comparison between the structural stability of perovskite thin films. Variation of the PL spectra of (a) $BDASnI_4$ and (b) $(PEA)_2SnI_4$ thin films with the number of mechanical exfoliations. The fresh perovskite films fixed on a platform were peeled off by pressing the 3M adhesive tape to them and then peeling the tape

away at an angle of 180° to the film surfaces. The PL spectra of the remained perovskite films were recorded after each peeling.

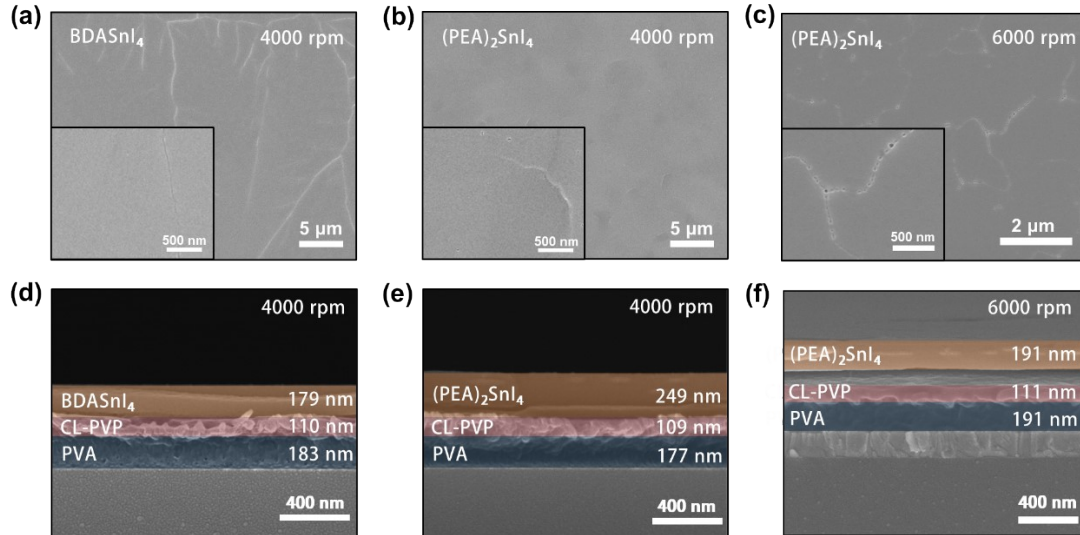


Figure S12. (a-c) Top-view SEM images at low and high magnifications and (d-f) cross-sectional SEM images of BDASnI₄ and (PEA)₂SnI₄ thin films on the polymer PVA/CL-PVP dielectric bilayers. The BDASnI₄ thin films were prepared at 4000 rpm. The (PEA)₂SnI₄ thin films were prepared at 4000 and 6000 rpm, respectively. The (PEA)₂SnI₄ film in (f) is peeled from the CL-PVP layer by the electron beam of the scanning electron microscope.

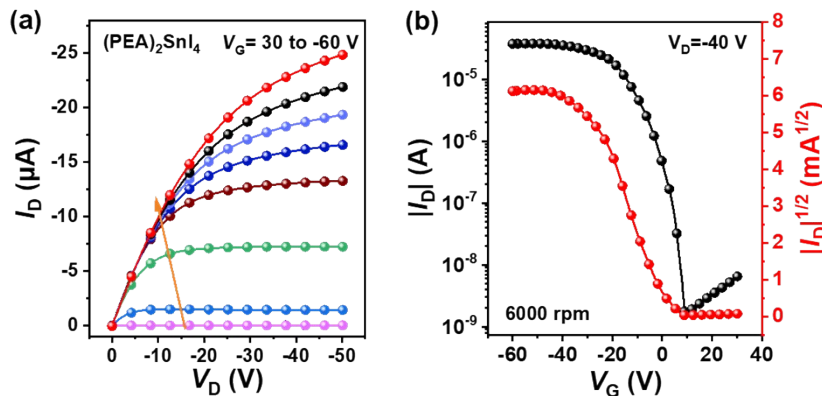


Figure S13. (a) Output and (b) transfer characteristics of (PEA)₂SnI₄ FETs. The (PEA)₂SnI₄ thin films were spin coated at 6000 rpm.

Table S9. Performance parameters and maximum interface trap densities of (PEA)₂SnI₄ FETs. The averaged values and standard deviations in parentheses are derived from every ten devices, respectively.

| Perovskite | Thickness (nm)/ Rotation Speed (rpm) | Mobility (cm ² V ⁻¹ S ⁻¹) | Threshold Voltage (V) | On-to-Off | Subthreshold | Interface Trap |
|-------------------------------------|---|--|--------------------------|---------------------|--------------------------------|---|
| | | | | Current Ratio | Swing (Vdec ⁻¹) | Density (cm ⁻² eV ⁻¹) |
| (PEA) ₂ SnI ₄ | 249/4000 | 0.33 (0.32±0.04) | 4.60 (5.05±3.73) | 5.0×10 ⁴ | 5.4 | 6.5×10 ¹² |
| (PEA) ₂ SnI ₄ | 191/6000 | 0.32 (0.30±0.03) | 3.35 (2.82±1.38) | 2.7×10 ⁴ | 3.1 | 3.7×10 ¹² |

Table S10. Mobility values estimated from the transfer curves of three scan cycles for BDASnI₄ and (PEA)₂SnI₄ FETs in Fig. 4.

| Perovskite | Mobility (cm ² V ⁻¹ S ⁻¹) | | |
|-------------------------------------|---|-------------|------------|
| | First Scan | Second Scan | Third Scan |
| BDASnI ₄ | 0.46 | 0.46 | 0.46 |
| (PEA) ₂ SnI ₄ | 0.29 | 0.32 | 0.40 |

Interfacial trap density

The maximum interfacial trap density of a perovskite FET is evaluated by:¹⁴

$$N = \left[\frac{SS \cdot \log e}{k_B T / q} - 1 \right] \frac{C_i}{q} \quad (\text{S8})$$

where SS is the subthreshold swing of the FET and C_i is the specific capacitance of the gate dielectric.

References

- 1 W. Zhou, H. Tang, D. Li, D. Zhang, H. Zhang, A. Yang and C. Liang, *Journal of Alloys and Compounds*, 2021, **856**, 157391.
- 2 Z. Xu, M. Chen and S. F. Liu, *J Phys Chem Lett*, 2019, **10**, 3670-3675.
- 3 H. Zhang, D. Li, B. Liu, Y. Ma, W. Zhou, D. Zhang, H. Tang, A. Yang and C. Liang, *The Journal of Physical Chemistry C*, 2020, **124**, 6796-6810.
- 4 L. Z. Wang, Y. Q. Zhao, B. Liu, L. J. Wu and M. Q. Cai, *Phys Chem Chem Phys*, 2016, **18**, 22188-22195.

- 5 I. Chung, J. H. Song, J. Im, J. Androulakis, C. D. Malliakas, H. Li, A. J. Freeman, J. T. Kenney and M. G. Kanatzidis, *J Am Chem Soc*, 2012, **134**, 8579-8587.
- 6 L.-J. Wu, Y.-Q. Zhao, C.-W. Chen, L.-Z. Wang, B. Liu and M.-Q. Cai, *Chinese Physics B*, 2016, **25**, 107202.
- 7 A. Z. Su-Huai Wei, *PHYSICAL REVIEW B*, 1999, **60**, 5404.
- 8 U.-G. Jong, C.-J. Yu, J.-S. Ri, N.-H. Kim and G.-C. Ri, *Physical Review B*, 2016, **94**, 125139
- 9 T. Schultz, T. Lenz, N. Kotadiya, G. Heimel, G. Glasser, R. Berger, P. W. M. Blom, P. Amsalem, D. M. de Leeuw and N. Koch, *Advanced Materials Interfaces*, 2017, **4**, 1700324.
- 10 Y. Jiang, M. Cui, S. Li, C. Sun, Y. Huang, J. Wei, L. Zhang, M. Lv, C. Qin, Y. Liu and M. Yuan, *Nat Commun*, 2021, **12**, 336.
- 11 B. Zhao, G. Niu, Q. Dong, J. Liu, N. Li, J. Li and L. Wang, *Journal of Materials Chemistry A*, 2018, **6**, 23797-23804.
- 12 S. Y. Smolin, M. D. Scafetta, G. W. Guglietta, J. B. Baxter and S. J. May, *Applied Physics Letters*, 2014, **105**, 022103.
- 13 Z. Wang, F. Wang, B. Zhao, S. Qu, T. Hayat, A. Alsaedi, L. Sui, K. Yuan, J. Zhang, Z. Wei and Z. Tan, *J Phys Chem Lett*, 2020, **11**, 1120-1127.
- 14 W. L. Kalb and B. Batlogg, *Physical Review B*, 2010, **81**, 035327.